

Optimized moth-eye anti-reflective structures for As₂S₃ chalcogenide optical fibers

R. J. Weiblen,^{1,*} C. R. Menyuk,¹ L. E. Busse,² L. B. Shaw,²
J. S. Sanghera,² and I. D. Aggarwal³

¹Department of Computer Science and Electrical Engineering, TRC 203, University of Maryland Baltimore County, 1000 Hilltop Circle, Baltimore, MD 21250, USA

²Naval Research Laboratory, Code 5620, Washington, D.C. 20375, USA

³Sotera Defense Solutions, Crofton, MD 21114, USA

*ro2@umbc.edu

Abstract: We computationally investigate moth-eye anti-reflective nanostructures imprinted on the endfaces of As₂S₃ chalcogenide optical fibers. With a goal of maximizing the transmission through the endfaces, we investigate the effect of changing the parameters of the structure, including the height, width, period, shape, and angle-of-incidence. Using these results, we design two different moth-eye structures that can theoretically achieve almost 99.9% average transmission through an As₂S₃ surface.

© 2016 Optical Society of America

OCIS codes: (050.6624) Subwavelength structures; (060.2390) Fiber optics, infrared.

References and links

1. Lord Rayleigh, "On reflection of vibrations at the confines of two media between which the transition is gradual," *Proc. London Math. Soc.* **S1-11**, 51–56 (1879).
2. C. G. Bernhard and W. H. Miller, "A corneal nipple pattern in insect compound eyes," *Acta Physiol. Scand.* **56**, 385–386 (1962).
3. D. G. Stavenga, S. Foletti, G. Palasantzas, and K. Arikawa, "Light on the moth-eye corneal nipple array of butterflies," *Proc. Biol. Sci.* **273**, 661–667 (2006).
4. S. Chattopadhyay, Y. F. Huang, Y. J. Jen, A. Ganguly, K. H. Chen, and L. C. Chen, "Anti-reflecting and photonic nanostructures," *Materials Sci. Eng. Rev.* **69**, 1–35 (2010).
5. J. Kulakofsky, W. Lewis, M. Robertson, T. Moore, and G. Krishnan, "Designing high-power components for optical telecommunications," *Proc. SPIE* **4679**, 198 (2002).
6. S. A. Boden and D. M. Bagnall, "Optimization of moth-eye antireflection schemes for silicon solar cells," *Prog. Photovolt: Res. Appl.* **18**, 195–203 (2010).
7. Y. Ou, D. Corell, C. Dam-Hansen, P. Petersen, and H. Ou, "Antireflective sub-wavelength structures for improvement of the extraction efficiency and color rendering index of monolithic white light-emitting diode," *Opt. Express* **19**, A166–A172 (2011).
8. D. S. Hobbs, B. D. MacLeod, and J. R. Riccobono, "Update on the development of high performance anti-reflecting surface relief micro-structures," *Proc. SPIE* **6545**, 65450Y (2007).
9. T. Hoshino, M. Itoh, and T. Yatagai, "Antireflective grating in the resonance domain for displays," *Appl. Opt.* **46**, 648–656 (2007).
10. J. Sanghera, C. Florea, L. Busse, L. B. Shaw, F. Miklos, and I. Aggarwal, "Reduced Fresnel losses in chalcogenide fibers by using anti-reflective surface structures on fiber end faces," *Opt. Express* **18**, 26760–26768 (2010).
11. N. H. Finkel, B. G. Prevo, O. D. Velev, and L. He, "Ordered silicon nanocavity arrays in surface-assisted desorption/ionization mass spectrometry," *Anal. Chem.* **77**, 1088–1095 (2005).
12. S. Y. Chou, P. R. Krauss, and P. J. Renstrom, "Nanoimprint lithography," *J. Vac. Sci. Technol. B* **14**, 4129–4133 (1996).
13. M. Kowalczyk, J. Haberko, and P. Wasylczyk, "Microstructured gradient-index antireflective coating fabricated on a fiber tip with direct laser writing," *Opt. Express* **22**, 12545–12550 (2014).

14. B. D. MacLeod, D. S. Hobbs, and E. Sabatino, "Moldable AR microstructures for improved laser transmission and damage resistance in CIRCUM fiber optic beam delivery systems," *Proc. SPIE* **8016**, 80160Q (2011).
15. R. J. Weiblen, C. Florea, A. Docherty, C. R. Menyuk, L. B. Shaw, J. Sanghera, L. Busse, and I. Aggarwal, "Optimizing motheye antireflective structures for maximum coupling through As_2S_3 optical fibers," in *IEEE Photonics Conference* (IEEE, 2012), paper ThP3.
16. K. Han and C.-H. Chang "Numerical modeling of sub-wavelength anti-reflective structures for solar module applications," *Nanomaterials* **4**, 87–128 (2014).
17. J. Yamauchi, M. Mita, S. Aoki, and H. Nakano, "Analysis of antireflection coatings using the FD-TD method with the PML absorbing boundary condition," *IEEE Photonics Technol. Lett.* **8**, 239–241 (1996).
18. Z. Y. Yang, D. Q. Zhu, M. Zhao, and M. C. Cao, "The study of a nano-porous optical film with the finite difference time domain method," *J. Opt. A: Pure Appl. Opt.* **6**, 564–568 (2004).
19. M. G. Moharam and T. K. Gaylord, "Rigorous coupled-wave analysis of planar-grating diffraction," *J. Opt. Soc. Am.* **71**, 811–818 (1981).
20. L. Li, "New formulation of the Fourier modal method for crossed surface-relief gratings," *J. Opt. Soc. Am. A* **14**, 2758–2767 (1997).
21. D. S. Hobbs, B. D. MacLeod, E. Sabatino III, T. M. Hartnett, and R. L. Gentilman, "Laser damage resistant anti-reflection microstructures in Raytheon ceramic YAG, sapphire, ALON, and quartz," *Proc. SPIE* **8016**, 80160T (2011).
22. D. S. Hobbs, "Laser damage threshold measurements of anti-reflection microstructures operating in the near UV and mid-IR," *Proc. SPIE* **7842**, 78421Z (2010).
23. C. Florea, L. Busse, S. Bayyab, B. Shaw, I. Aggarwal, and J. Sanghera, "Anti-reflective surface structures in spinel ceramic windows," in *The 10th Pacific Rim Conference on Ceramic and Glass Technology* (2013), paper S10-014.
24. L. Busse, C. Florea, L. B. Shaw, S. Bayya, G. Villalobos, I. Aggarwal, and J. Sanghera, "Anti-reflective surface structures for high energy laser applications," in *Annual Directed Energy Symposium* (2013), paper 13-Symp-053.
25. R. J. Weiblen, C. Florea, L. Busse, L. B. Shaw, C. R. Menyuk, I. Aggarwal, and J. Sanghera, "Irradiance enhancement and increased laser damage threshold in As_2S_3 moth-eye antireflective structures," *Opt. Lett.* **40**, 4799–4802 (2015).
26. R. J. Weiblen, C. Florea, C. R. Menyuk, I. Aggarwal, L. Busse, L. B. Shaw, and J. Sanghera, "Ideal cusp-like motheye antireflective structures for chalcogenide optical fibers," in *IEEE Photonics Conference* (2015), paper W11.4.
27. A. F. Oskooi, D. Roundy, M. Ibanescu, P. Bermel, J. D. Joannopoulos, and S. G. Johnson, "MEEP: a flexible free-software package for electromagnetic simulations by the FDTD method," *Comp. Phys. Comm.* **181**, 687–702 (2010).
28. D. Raguin and G. Morris, "Antireflection structured surfaces for the infrared spectral region," *Appl. Opt.* **32**, 1154–1167 (1993).
29. M. Steel, T. White, C. M. de Sterke, R. McPhedran, and L. Botten, "Symmetry and degeneracy in microstructured optical fibers," *Opt. Lett.* **26**, 488–490 (2001).
30. W. H. Southwell, "Pyramid-array surface-relief structures producing antireflection index matching on optical surfaces," *J. Opt. Soc. Am. A* **8**, 549–553 (1991).

1. Introduction

It has been known since the time of Lord Rayleigh that microscale structures on the surface of optical interfaces are effective at reducing Fresnel reflections [1]. Periodic anti-reflective (AR) microstructures are called "moth-eye" structures because of their similarity to the microstructures on the eyes of nocturnal moths [2, 3]. Moth-eye structures are a biomimetic microstructured AR surface structure that are effective at reducing Fresnel reflections [4]. In the long wavelength limit, they work by providing a gradual change of the effective refractive index as light propagates across the air-glass interface. They are especially useful for high-index materials, which includes most mid-IR materials, such as chalcogenide glasses. Reducing Fresnel reflections from optical interfaces is important in mid-IR applications, where high power and low loss are needed. High power laser radiation that reflects from interfaces can damage instruments, while insertion or coupling losses can be major contributors to overall losses in a system [5]. Hence, mid-IR systems can benefit greatly by using moth-eye structures to reduce reflections from and increasing transmission through interfaces. They are useful in a number of applications, including laser systems [5], photovoltaics [6], LEDs [7], automotive glass [8],

electronics displays [9], and fiber optics [10].

Moth-eye structures can be imprinted by numerous methods, including wet or dry etching [11], nanoimprint lithography [12], or direct laser writing [13]. Sanghera et al. [10] and MacLeod et al. [14] recently demonstrated a direct stamping method for nanoimprinting moth-eye structures on the end-faces of chalcogenide optical fibers, where AR interfaces are particularly useful because of the large refractive index difference between air and As_2S_3 (~ 2.45 at a wavelength of $\lambda = 2 \mu\text{m}$). The direct stamping method allows structures to be accurately replicated, and the reflection as a function of wavelength depends sensitively on the structures and their parameters [15], which means that they must be accurately modeled. Because in the structures studied in this work, the microstructure feature dimensions are on the same order as the wavelength of the incoming radiation ($\sim 1 \mu\text{m}$), light in adjacent features interacts, and thus neither the long-wavelength average refractive index model nor the short-wavelength ray optics model is appropriate to describe transmission through moth-eye structures. Hence, they must be modeled using rigorous computational methods [16], such as the finite-element method (FEM), the finite-difference time-domain method (FDTD) [17, 18], or rigorous coupled-wave analysis (RCWA) [19, 20], where the results become exact in principle as the grid size and step size tend to zero (FEM and FDTD) or the number of harmonics becomes infinite (RCWA). We have simulated moth-eye structures using three methods, FEM, FDTD and RCWA. We find that they agree perfectly, but that RCWA is the fastest and most accurate method.

Moth-eye structures have several advantages over traditional thin-film AR coatings, including environmental tolerance, surface adhesion, single material fabrication, minimal surface preparation, and self-cleaning via the lotus effect [8, 10]. Additionally, in recent years it has been shown that in many cases periodic moth-eye structures have a higher laser-induced damage threshold (LIDT) than do traditional AR-coated surfaces [21–24]. We explained this effect in terms of the boundary conditions for Maxwell's equations [25].

In this work, we optimize the shape and dimensions of moth-eye structures for maximum input and output coupling through the endfaces of As_2S_3 optical fibers. We previously presented some of these results in brief meeting reports [15, 26], but here we show an in-depth investigation of all relevant moth-eye structure parameters, including the structure shape, dimensions, period, packing, and the angle-of-incidence. The rest of this paper is organized as follows: In Sec. 2, we verify our theoretical model by comparing our results to experimentally-measured results. In Secs. 3–5, we report our investigations of the effects of changing the dimensions and period of the moth-eye structures (Sec. 3), changing the angle-of-incidence of the input radiation (Sec. 4), and changing the shape of the moth-eye structure (Sec. 5). We have used the insights of Secs. 2–5 to design and optimize moth-eye structures with nearly ideal 100% transmission, and we report these designs in Sec. 6. Finally, Sec. 7 contains the conclusions.

2. Comparison of computer simulations and experiment

The goal of the work described in this section is to create and validate a theoretical model that agrees with the results for a particular moth-eye structure that was experimentally studied by Sanghera et al. [10] and is shown in Fig. 1(c). We calculate the transmission of the structured surface by simulating a plane-wave incident upon an As_2S_3 structured surface transmitting medium using the open-source finite-difference time-domain (FDTD) computer software MEEP [27]. The simulation propagates a wave-packet of specific bandwidth from a vacuum incident medium through the microstructure and then calculates the transmission and reflection spectra by taking a harmonic transform of the time-domain flux through measurement surfaces that are situated above and below the microstructured surface. We use a spatial resolution of 10 nm for all simulations, and we have verified that increasing the resolution does not affect the results. We utilize the periodicity of the structure and only solve for the fields in a single unit

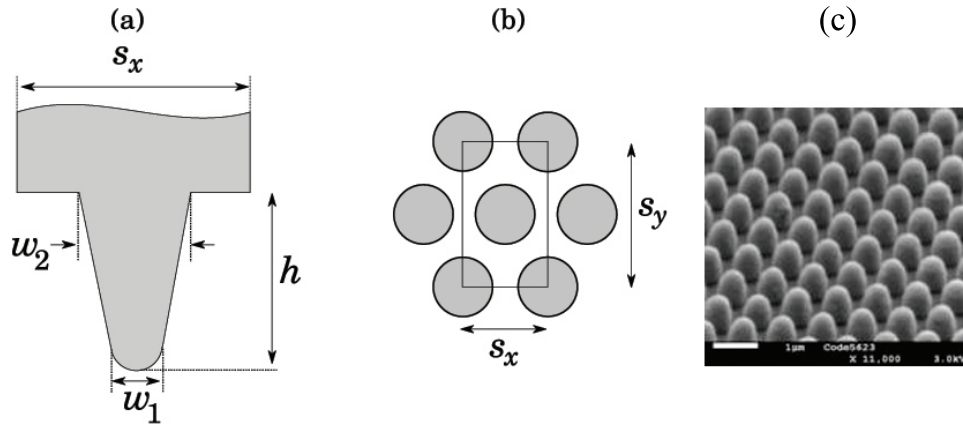


Fig. 1. Schematic view of a moth-eye cone structure: (a) Side cross-section view; (b) top view showing a unit cell; (c) SEM with 1- μm scale-bar.

cell, using Floquet-Bloch boundary conditions. Additionally, for circularly symmetric structures in a square or hexagonal packing scheme with normal incidence, it is sufficient to study a single polarization of incoming light, since the results do not depend on the polarization in that case [28, 29]. The calculated transmission spectra have been verified by comparison with the commercial software package DiffractMOD[®] by RSOFT, which uses the rigorous coupled wave algorithm (RCWA).

The experimental transmission spectrum was measured at the Naval Research Laboratory. In the experiment, the fiber end face was embossed with a moth-eye structure using a shim with the negative of the desired moth-eye pattern. The transmission through the fiber before and after the moth-eye structure was applied were tested using an FTIR spectrometer. Details of the experimental set up to fabricate the moth-eye structure as well as the measurements are given in detail in [10].

The experimental shape is modeled by a truncated cone with a hemispheric cap that is fully determined by specifying the cone height, h ; the base diameter, w_2 ; the tip diameter, w_1 ; and the lattice constant of the packing, s_x . Since the features are hexagonally packed, $s_y = \sqrt{3}s_x$. These geometric parameters are shown diagrammatically in Figs. 1(a) and 1(b). The cone approximation to the experimentally-implemented feature has the following parameters, which can be determined from the SEM image. $w_1 = 0.2 \mu\text{m}$, $w_2 = 0.7 \mu\text{m}$, $h = 0.9 \mu\text{m}$, $s_x = 0.92 \mu\text{m}$, and $s_y = 1.59 \mu\text{m}$. For all theoretical models, we set the refractive index n of As_2S_3 to be equal to $n = 2.45$, which is a good approximation to the experimentally-measured value over the wavelength range of interest.

The calculated transmission spectra are shown in Fig. 2 for light that is coupled into and out of an optical fiber. The spectra are very similar at longer wavelengths and differ for shorter wavelengths for reasons that will be explained shortly. The output coupling exhibits a sharp falloff at short wavelengths, while the input coupling does not. The transition from high to low transmission as the wavelength decreases is called the diffraction edge, is sharp, and occurs at $1.9 \mu\text{m}$ for this structure.

Figure 2 also shows that the experimentally-measured transmission for light coupled out of the fiber and the drop-off in transmission for shorter wavelengths match the theoretical result. The measured transmission spectrum is somewhat lower at longer wavelengths, which could be caused by a slightly different cone shape in the experimental system than in our theoretical model and/or by material losses, which are not included in our theoretical model.

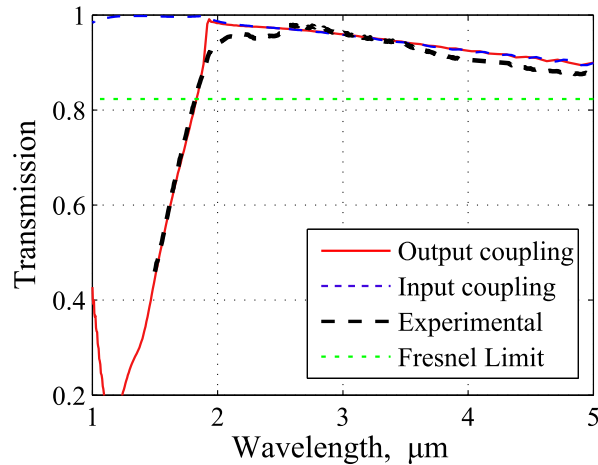


Fig. 2. The theoretical transmission spectra of light coupled into and coupled out of the fiber. The experimental transmission spectrum of light coupled out of the fiber is also shown. The Fresnel limit is the transmission spectrum from a plane-wave coupling into or out of a fiber with a flat end-face.

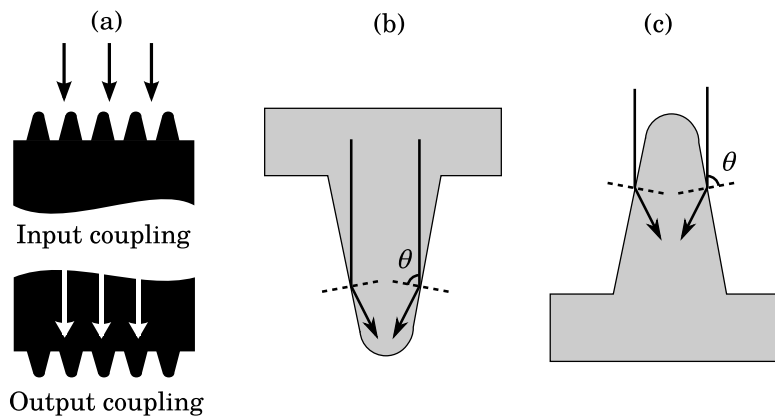


Fig. 3. (a) Coupling of light into and out of the fiber represented graphically. The ray-optics pictures of light coupling (b) out of the structure, and (c) into the structure.

Finally, Fig. 2 shows the transmission through a bare fiber end-face with no AR structure for comparison. The Fresnel-limited transmission depends only on the refractive indices of the incident and transmitting medium and, in this case, is approximately 83%.

2.1. Coupling into and out of a fiber

The coupling of light into the fiber and the transmission out of the fiber are two different problems, as schematically shown in Fig. 3(a). For long wavelengths, the behavior of both input and output coupling can be expected to be similar, as the electro-magnetic field will average over the moth-eye surface, effectively homogenizing the refractive index transition and leading to similar transmission properties in both directions.

For shorter wavelengths, we expect the transmission properties to be very different. In the

ray-optics limit, normally incident light will be totally internally reflected inside the cones in the output coupling case, whereas light will be refracted directly into the fiber in the input coupling case, as shown in Figs. 3(b) and 3(c). Total internal reflection occurs when the angle that the incident light ray makes with the cone surface, θ , is greater than the critical angle, 24° , as is the case with all of the practical cone designs considered.

This argument gives an intuitive picture of how a structured surface can yield very different behavior for light coupled into and out of the high index material. However, the coupling at wavelengths close to the size of the structure is complicated due to the interaction of the electromagnetic field in adjacent cone structures. The wavelength at which the input and output coupling differ is called the diffraction edge, because for wavelengths below the diffraction edge, diffracted orders greater than zero exist in the transmitted spectrum. Full numerical simulations of Maxwell's equations are therefore required to obtain a qualitative picture of the transmission spectra as well as a quantitative result.

3. Changing the dimensions

Next, we investigate changing the dimensions of the truncated cone to determine the effect on the transmission spectrum. We vary each parameter independently, starting with the tip width.

3.1. Tip width

The calculated transmission spectra for input and output coupling for different values of the cone tip diameter, w_1 , are shown in Fig. 4. All other parameters are kept fixed at $w_2 = 0.7 \mu\text{m}$, $h = 0.9 \mu\text{m}$, $s_x = 0.92 \mu\text{m}$, and $s_y = 1.59 \mu\text{m}$.

As the cone tip diameter is increased from $w_1 = 0.1 \mu\text{m}$ to $w_1 = 0.7 \mu\text{m}$, the transmission for wavelengths above $3.5 \mu\text{m}$ increases. However, for wavelengths around $2.8 \mu\text{m}$, the transmission correspondingly decreases. For output coupling, the transmission drop-off near $2 \mu\text{m}$ does not change significantly for different values of w_1 . For input coupling, the transmission decreases below $2 \mu\text{m}$ as the tip diameter increases.

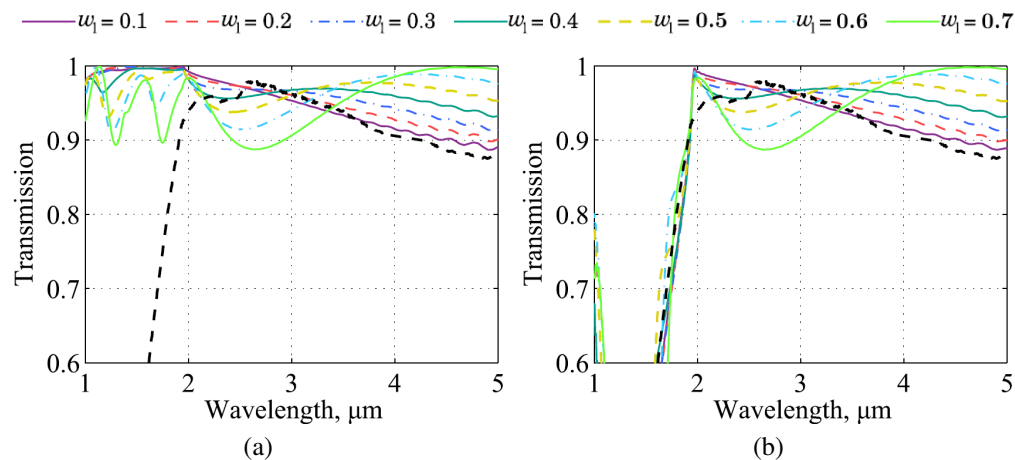


Fig. 4. The transmission spectra of light coupled (a) into and (b) out of the fiber as the cone tip diameter w_1 varies. The other geometric parameters are $w_2 = 0.7 \mu\text{m}$, $h = 0.9 \mu\text{m}$, and $s_x = 0.92 \mu\text{m}$. The experimental transmission spectrum of light coupled out of the fiber is shown for comparison (black dashed line).

3.2. Base width

In the second parameter study, we varied the diameter of the base of the cone, keeping the other parameters fixed at $w_1 = 0.2 \mu\text{m}$, $h = 0.9 \mu\text{m}$, and $s_x = 0.92 \mu\text{m}$. The resulting transmission spectra versus wavelength are shown in Fig. 5. We see that for very narrow cones, with $w_2 = 0.3 \mu\text{m}$, the transmission is only slightly increased above the Fresnel limit of a flat interface, which is approximately 83%. For both input and output coupling, the slopes of the transmission spectra become increasingly steep, decreasing from almost 100% transmission near $2.5 \mu\text{m}$ to around 92% transmission near $5 \mu\text{m}$ at the largest base diameter that we consider, $w_2 = 0.9 \mu\text{m}$, where the base of the cones would be almost touching. For input coupling we see that as w_2 increases, the transmission increases for all wavelengths. Furthermore, for output coupling, we find that as w_2 increases, the cutoff at $2 \mu\text{m}$ becomes stronger.

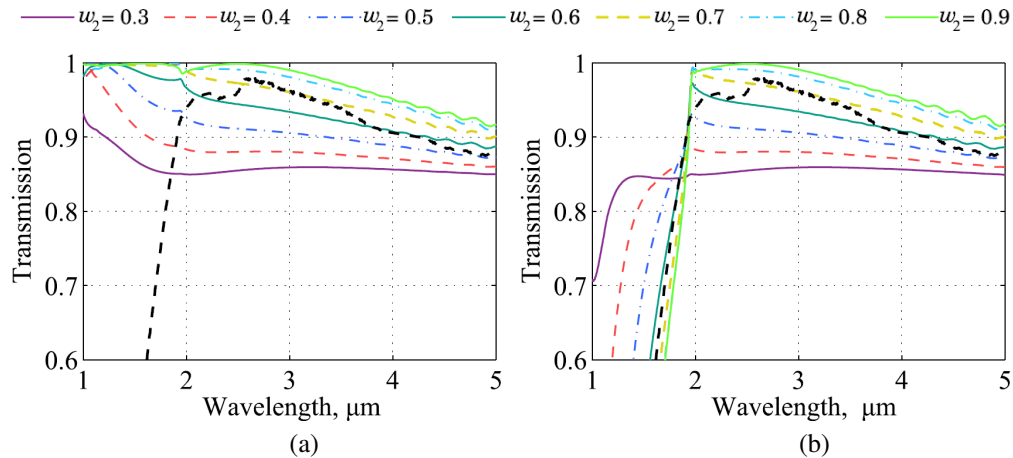


Fig. 5. The transmission spectra of light coupled (a) into and (b) out of the fiber versus the cone bottom diameter w_2 . The other geometric parameters are $w_1 = 0.2 \mu\text{m}$, $h = 0.9 \mu\text{m}$, and $s_x = 0.92 \mu\text{m}$. The experimental transmission spectrum of light coupled out of the fiber is shown for comparison (black dashed line).

3.3. Height

The transmission spectra versus wavelength for different cone heights, h , are shown in Fig. 6. All other parameters are kept fixed at $w_1 = 0.2 \mu\text{m}$, $w_2 = 0.7 \mu\text{m}$, $s_x = 0.92 \mu\text{m}$, and $s_y = 1.59 \mu\text{m}$. The transmission above $3.5 \mu\text{m}$ increases as the cone height increases; however, the transmission also decreases slightly with increasing h near a wavelength of $3 \mu\text{m}$. The same behavior is seen for both input and output coupling. The height does not greatly affect the transmission below $2 \mu\text{m}$ for input coupling; for output coupling the transmission increases, although it is still considerably below the Fresnel limit of 83%, and the sharp cutoff is still present.

3.4. Period

The final geometric parameter that we change in our model is the lattice spacing or the period of the cones, s_x . The lattice packing is kept hexagonal; deviations from this packing by choosing s_y differently would cause different polarizations of light to have different transmission spectra [28, 29]. All other parameters are kept fixed at $w_1 = 0.2 \mu\text{m}$, $w_2 = 0.7 \mu\text{m}$, $h = 0.9 \mu\text{m}$. The results are shown in Fig. 7. We find that the transmission increases with decreasing s_x . This re-

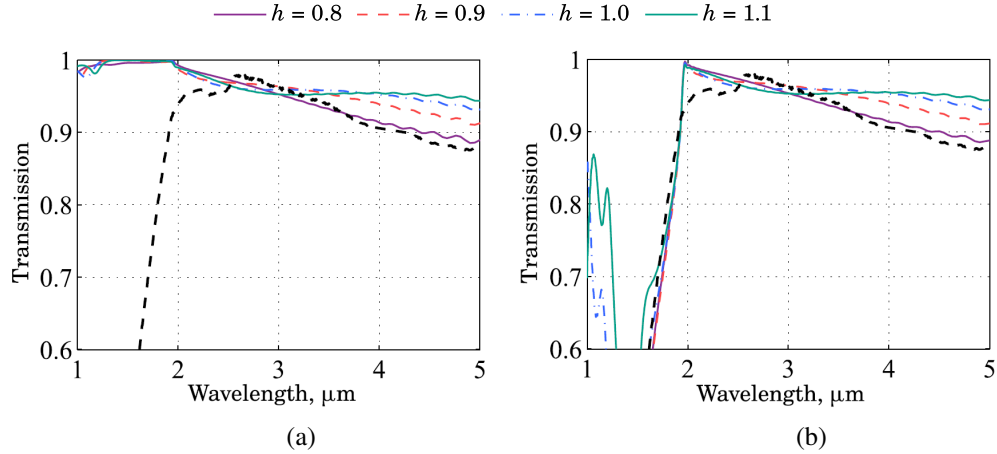


Fig. 6. The transmission spectra of light coupled (a) into and (b) out of the fiber versus the cone height h . The experimental transmission spectrum of light coupled out of the fiber is shown for comparison (black dashed line).

sult qualitatively agrees with the results of changing the cone base diameter: In both cases, the packing density of the cones increases, causing the interaction of the fields between cones to increase, which in turn increases the resulting transmission. The results for output coupling are shown in Fig. 7(b). In this case, we find that changing the lattice constant changes the cut-off or diffraction edge wavelength, which increases as s_x increases.

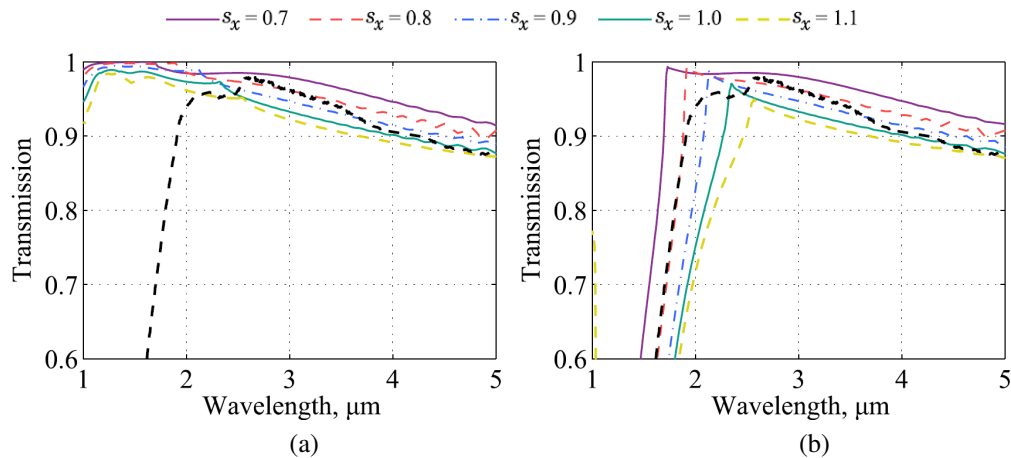


Fig. 7. The transmission spectra of light coupled (a) into and (b) out of the fiber versus the cone hexagonal packing spacing s_x . The experimental transmission spectrum of light coupled out of the fiber is shown for comparison (black dashed line).

4. Angle of incidence

The effect of changing the angle of incidence of the input plane wave is shown in Fig. 8 for angles up to 30° for the same moth-eye structure that was discussed in the previous section. For input coupling, the transmission spectrum is almost unaffected by changes in the angle

of incidence. This result makes sense conceptually, as argued previously from the ray picture in Fig. 3(c). For output coupling, the transmission drops significantly for angles of incidence above 10° , going to zero for wavelengths above $2 \mu\text{m}$ for an incidence angle of 30° .

For single mode fibers the low transmission at non-normal incidence for output coupling would not be a problem since the angle of incidence for the fundamental mode would be close to normal; however, for multimode fibers this issue should be taken into consideration.

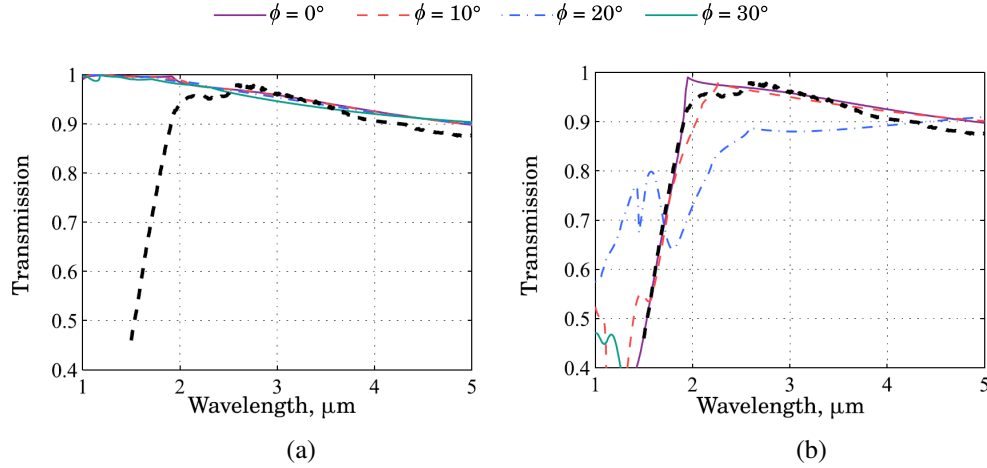


Fig. 8. The transmission spectra of light coupled (a) into and (b) out of the fiber versus the incidence angle of the input plane-wave, ϕ . The experimental transmission spectrum of light coupled out of the fiber is shown for comparison (black dashed line).

5. Changing the shape

In this section, we study the effect of changing the shape of the moth-eye structure element. The shapes we study are a half-ellipsoidal shape, a sinusoidal shape, and a truncated pyramid. The truncated pyramid element is a flat-sided square pyramid with the top cut off. The half-ellipsoid structure is the upper half of an ellipsoid oriented along the z -axis, whose height is given by the equation

$$z(x, y) = h \left[1 - \left(\frac{x}{w_2/2} \right)^2 - \left(\frac{y}{w_2/2} \right)^2 \right]^{1/2}, \quad (1)$$

where x and y are the axes parallel to the surface, z is the height perpendicular to the surface, h is the element height, and w_2 is the base width. The sinusoidal shape is given by the upper half of a cosine rotated around the z -axis, which has a height

$$z(x, y) = h \cos \left\{ \frac{\pi}{w_2} \left[\left(\frac{x}{w_2/2} \right)^2 + \left(\frac{y}{w_2/2} \right)^2 \right]^{1/2} \right\}, \quad (2)$$

where again x and y denote the axes that are parallel to the surface, z denotes the height perpendicular to the surface, h is the element height, and w_2 is the base width. We show cross sections of each feature shape in Figs. 9(a)–(c).

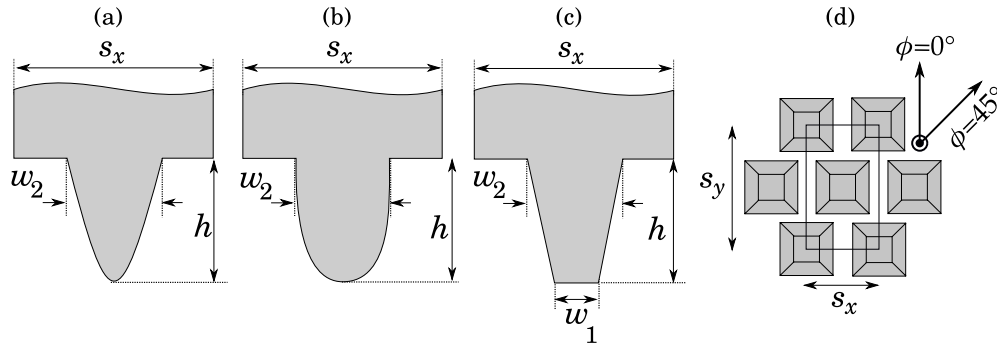


Fig. 9. Cross-section of (a) a sinusoidal structure, (b) a half-ellipsoid structure, and (c) a truncated pyramid structure. (d) The pyramidal surface from the top, showing the polarization angles used in the simulations.

5.1. Positive structures

First, we studied positive structures formed from these element shapes. Positive structures correspond to the gray areas in Fig. 9 being As_2S_3 , with the white areas (background) being air. We compare the transmission spectra for positive elements of three different heights $h = 0.8 \mu\text{m}$, $1.2 \mu\text{m}$, and $1.6 \mu\text{m}$ and two base widths of $w_2 = 0.7 \mu\text{m}$ and $0.9 \mu\text{m}$. The pyramidal element has an extra parameter compared to the sinusoidal and half-ellipsoid elements, which is the top width w_1 ; for the following calculations, we set $w_1 = 0.15 \mu\text{m}$. The pyramidal structure is also not rotationally symmetric about the z -axis, unlike the other two structures, and will therefore have different transmission properties depending on the polarization of the incident light.

The calculated transmission spectra in the case of output coupling for the sinusoidal and half-ellipsoid surfaces are shown in Figs. 10(a) and 10(b) respectively. For the sinusoidal surface, the transmission is greater for larger base widths. The transmission is generally flatter for taller elements, although there is little change between $h = 1.2 \mu\text{m}$ and $h = 1.6 \mu\text{m}$. For the half-ellipsoid surface, the transmission is greater for larger base widths and is flatter for taller elements, and the highest transmission is obtained when the element is widest and has a height $h = 1.2 \mu\text{m}$ or $h = 1.6 \mu\text{m}$. However, for the half-ellipsoid surface with $w_2 = 0.7 \mu\text{m}$, as the height is increased, the transmission actually drops below the transmission for shorter elements. A similar dip occurs with the sinusoid surface, but it is less significant.

The calculated transmission spectra for the pyramidal surface are shown in Fig. 11(a). The highest and widest pyramidal structure of $h = 1.6 \mu\text{m}$ and $w_2 = 0.9 \mu\text{m}$ performs the best of all the shapes considered and has a transmission of almost unity across the wavelength range $\lambda = 2\text{--}5 \mu\text{m}$.

Figure 11(b) shows the transmission for different polarization states of the incoming electric field. A polarization angle of $\phi = 0^\circ$ corresponds to the electric field parallel to the sides of the base of the pyramidal and a polarization angle of $\phi = 45^\circ$ corresponds to the electric field aligned diagonally to the base of the pyramidal, as shown in Fig. 9(d). The transmission drops slightly when $\phi = 45^\circ$, compared to when $\phi = 0^\circ$. We expect that the transmission for all other polarizations lies in between these extreme cases.

In most cases, we found that increasing the base width and height of the element increased the transmission across the wavelength range. However, this behavior was not found for all element shapes in all height ranges; for example, the transmission for the half-ellipsoid with base width of $w_2 = 0.7 \mu\text{m}$ is worse for taller elements. Also, for both the sinusoidal and half-ellipsoid elements, there is no improvement in transmission when the height increases from

$h = 1.2 \mu\text{m}$ to $h = 1.6 \mu\text{m}$. In fact, the transmission only increases for the pyramidal element with a base width $w_2 = 0.9 \mu\text{m}$ when the height is increased from $h = 1.2 \mu\text{m}$ to $h = 1.6 \mu\text{m}$. For the tallest and widest pyramid shape, the transmission is greater than 99.5% when the polarization angle $\phi = 0^\circ$ and 99% when $\phi = 45^\circ$ over the wavelength range $\lambda = 2\text{--}5 \mu\text{m}$. This transmission is the highest for all element shapes considered; however, with shorter element heights, the transmission for the pyramidal shape is not better than the other structures at longer wavelengths.

Different shapes have significantly different transmission spectra, even for two relatively similar smooth shapes like the sinusoid and the half-ellipsoid. Therefore, the exact shape of the elements is required to match experimental and theoretical calculations.

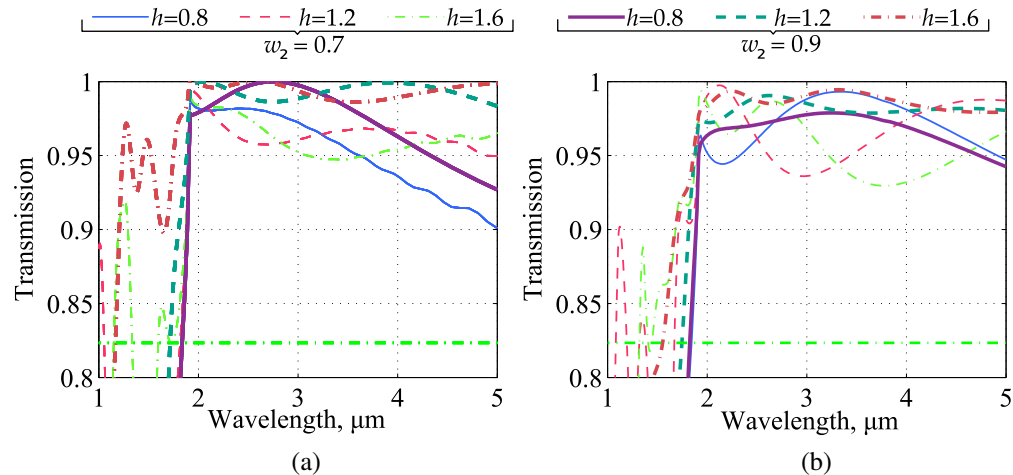


Fig. 10. The theoretical transmission spectra through a surface that consists of positive (a) sinusoidal structures and (b) ellipsoid structures, both with $w_2 = 0.7 \mu\text{m}$ (thin lines) and $w_2 = 0.9 \mu\text{m}$ (thick lines). The Fresnel transmission at around 83% is also shown for reference in both figures.

5.2. Negative structures

Here, we consider two different negative structure shapes, sinusoidal and half-ellipsoid holes, which are shown schematically in Fig. 12. These structure shapes are similar to the shapes that we considered previously for positive surfaces, and the shapes are again specified by Eqs. 1 and 2; however, now z specifies the depth of the hole below the surface, rather than the height above it.

The negative structures are parameterized in the same way as the positive structures, using the base width, w_2 , and the depth, h . The lattice parameter is the same as previously used, $s_x = 0.9 \mu\text{m}$, and the structures are again hexagonally packed.

The results for the transmission in the case of coupling out of the fiber for the negative sinusoid and half-ellipsoid structures is shown in Figs. 13(a) and 13(b) respectively. The transmission is higher for the negative structures with width $w_2 = 0.9 \mu\text{m}$ than for the positive structures with $w_2 = 0.7 \mu\text{m}$ for both shapes. The transmission also increased as the width increased for the positive surface, but this increase is even more significant here. Increasing the structure depth does not significantly increase the transmission for most shapes. The notable exception is the half-ellipsoid surface with $w_2 = 0.9 \mu\text{m}$, where the transmission increases markedly as the structures depth increases, reaching a transmission of almost unity across the wavelength range

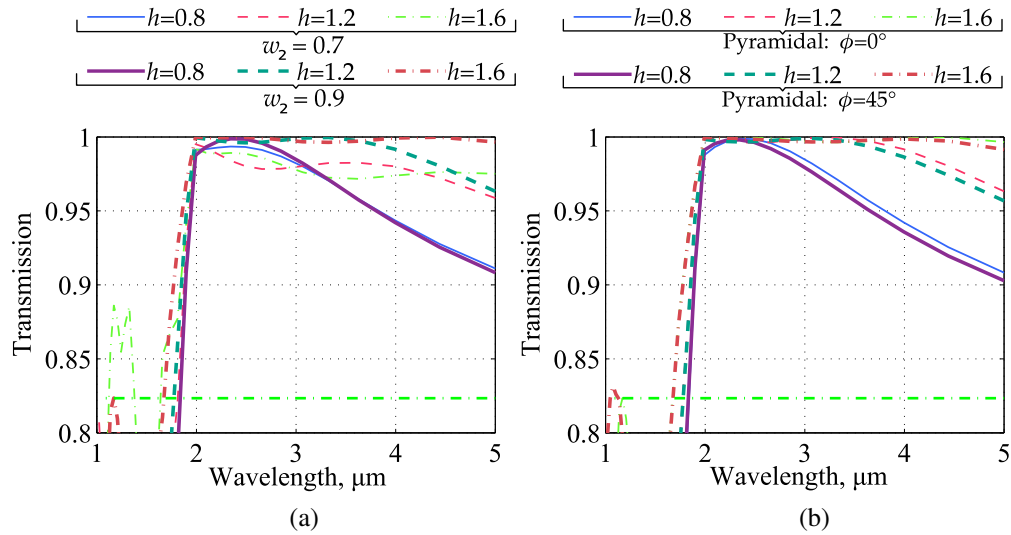


Fig. 11. The theoretical transmission spectra for a surface with positive pyramidal structures with $w_1 = 0.15 \mu\text{m}$, with (a) the electric field polarized fixed at $\phi = 0$ and the parameters $w_2 = 0.7 \mu\text{m}$ (thin lines) and $w_2 = 0.9 \mu\text{m}$ (thick lines); (b) the incident electric field polarized at $\phi = 0$ (thin lines) and $\phi = 45^\circ$ (thick lines) and the base width fixed at $w_2 = 0.9 \mu\text{m}$. The Fresnel transmission of 83% is also shown for reference in both figures.

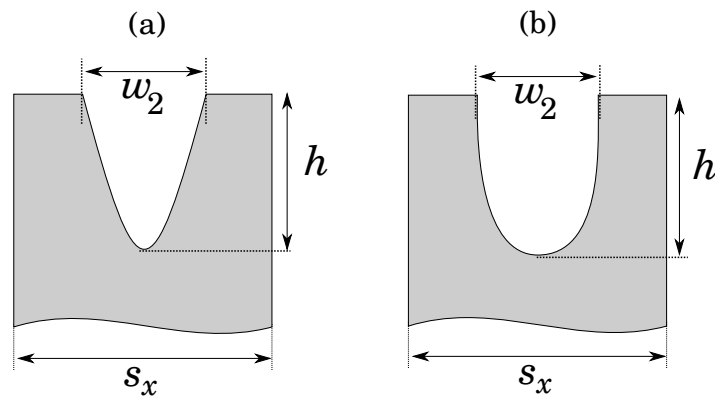


Fig. 12. Schematic view of a negative structured surface consisting of holes with (a) sinusoidal and (b) half-ellipsoid shapes.

above $\lambda = 2 \mu\text{m}$ for the deepest hole considered.

The surface with negative sinusoidal structures has a cut-off that is around $1.2 \mu\text{m}$ rather than $1.9 \mu\text{m}$, as is seen in the positive surface case, leading to a higher transmission in the wavelength range $\lambda = 1.2\text{--}1.9 \mu\text{m}$ for the sinusoidal surface, so that for the tallest and widest hole the transmission remains above 95% when $\lambda > 1.3 \mu\text{m}$. This increased cut-off is notable as the cut-off is tied to the periodicity of the lattice, and is not changed by any other factor for the positive surfaces. The tallest and widest negative half-ellipsoid structures also display an increased transmission in the cut-off region, as compared to the positive surface, only decreasing below 85% for wavelengths below $1.3 \mu\text{m}$.

The calculated transmission for coupling into the fiber for the two negative shapes is shown

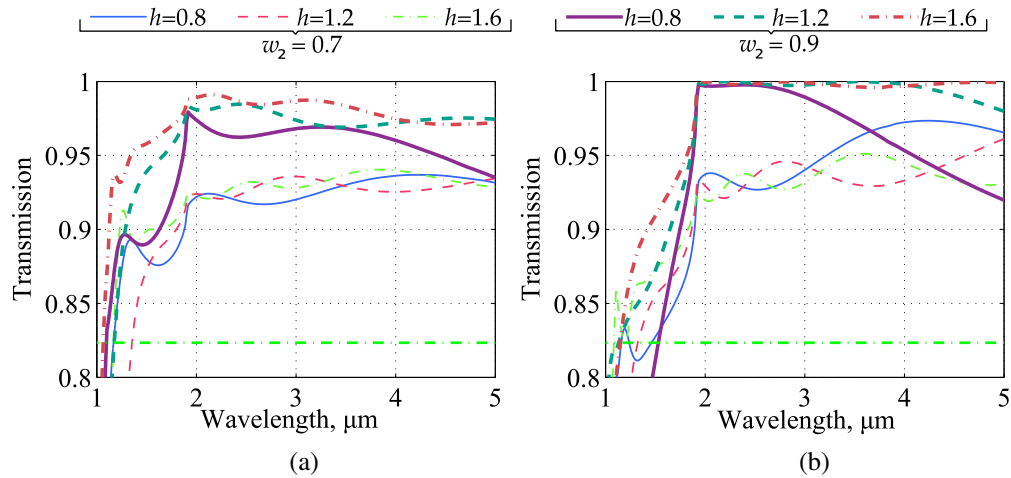


Fig. 13. The theoretical transmission spectra for *output* coupling through a negative structure surface consisting of structures with (a) sinusoidal and (b) half-ellipsoid shapes.

in Figs. 14(a) and 14(b) respectively. The transmission is the same as for coupling out of the fiber at wavelengths above 2 μm , but the spectra for input and output coupling diverge below 2 μm .

6. Optimized cusp-like moth-eye structures

In this section, we computationally study two different moth-eye structure shapes, half-ellipsoids and pyramids, to design an ideal moth-eye structure for maximum transmission in the wavelength range 2–5 μm , using insights gained from the previous sections. We find that the ideal structure, whether positive or negative, has a cusp-like glass tip and a smoothly increasing cross-sectional width that becomes equal to the period of the features. We show two examples of this kind of structure in Fig. 15.

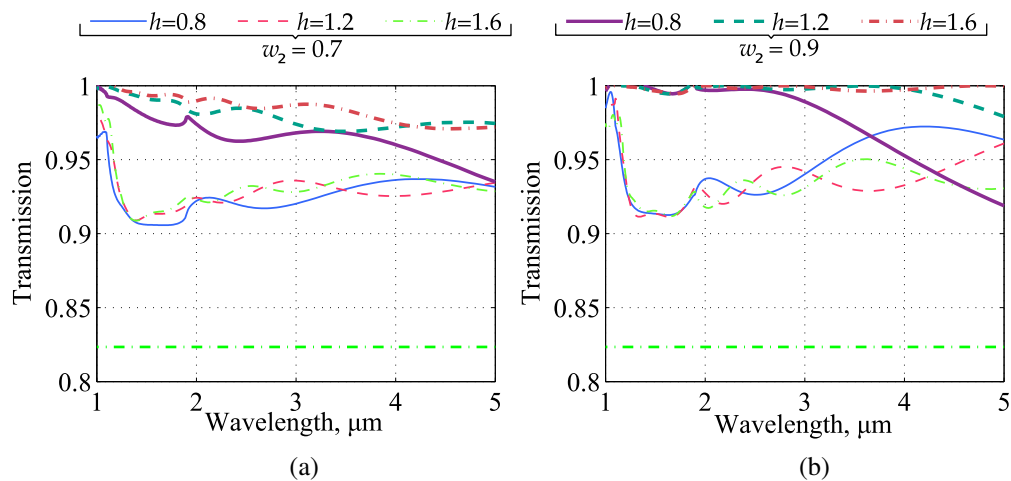


Fig. 14. The theoretical transmission spectra for *input* coupling through a negative structure surface consisting of structures with (a) sinusoidal and (b) ellipsoid shapes.

In the long wavelength limit, moth-eye structures provide a gradual change of the effective refractive index as light propagates across the air-glass interface, akin to an impedance transformer that matches the impedance of the optical surface to the impedance of the vacuum [28]. This long-wavelength limit picture is inexact, especially as the incident wavelength is on the order of the feature size, but it offers important insights that are useful for designing optimal structures.

The intuition provided by this picture suggests that the effective (average) refractive index of the layer at the highest point of the structure should be as close to that of the low index medium (air or vacuum in this case) as possible. Similarly, the bottom layer should have an effective index as close as possible to the index of the glass substrate. For layers in between, the effective refractive index should increase as gradually and as smoothly as possible. This intuition is consistent with our computational findings from Sec. 3.1–3.4.

6.1. Structure shapes

One way to create cusp-like structures is to imprint a negative structure in the glass with a positive mold that has a packing ratio $w_2/s_x = 1$, i.e. the width at the base of the mold (w_2) matches its feature spacing (s_x). Such a structure using a half-ellipsoid shape is shown in Fig. 15(a). The half-ellipsoid structure is the upper half of an ellipsoid oriented along the z -axis whose height is given by Eq. 1.

Another way to create such a cusp is to imprint a positive structure that comes to a fine point at its tip. One such structure, defined by Southwell [30] in terms of a quintic expression of the optical thickness of the structure, but without a closed-form expression, is shown in Fig. 15(b). This structure is not rotationally symmetric, and hence its transmissivity is anisotropic, but the anisotropy is small, as shown in Sec. 5.1. This structure is square-packed to make the base width equal to the feature spacing in both dimensions.

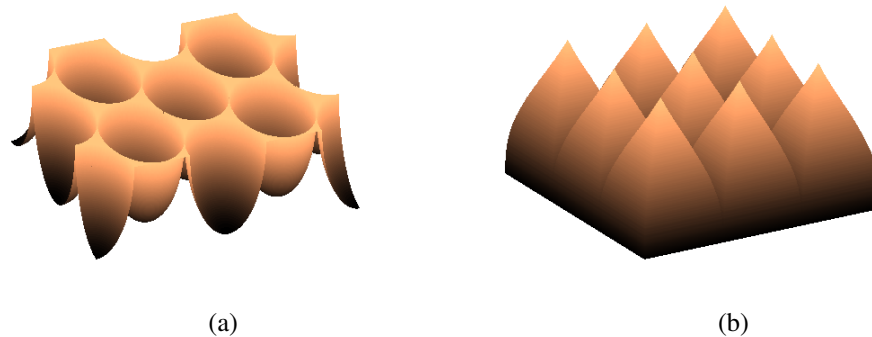


Fig. 15. Cusp-like moth-eye structure feature shapes: (a) Hexagonally-packed negative half-ellipsoid structures; (b) Square-packed positive pyramid structures.

6.2. Results

Figures 16 and 17 show the transmission spectra found by using rigorous coupled wave analysis (RCWA) for different element heights or depths and different ratios of base width to element period (w_2/s_x). Figure 16 shows the results for negative half-ellipsoids, and Fig. 17 shows the results for positive pyramids. Qualitatively, the highest transmissivity is obtained with the

tallest/deepest elements and for the highest ratio of w_2/s_x , which makes the negative features more cusp-like.

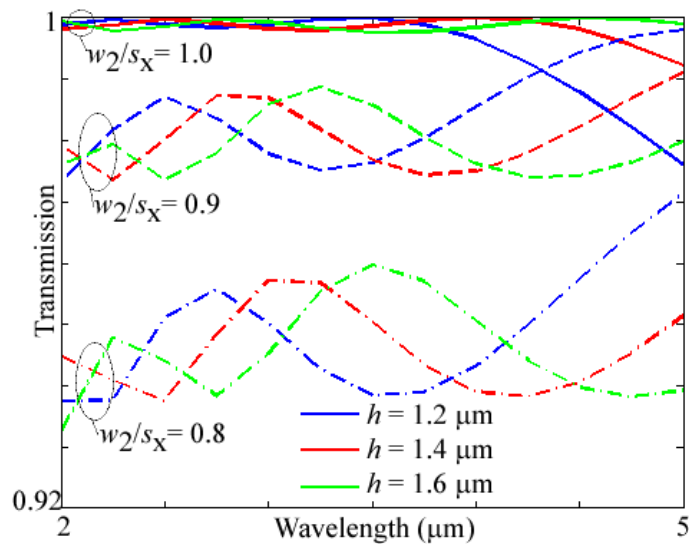


Fig. 16. Negative half-ellipsoid transmission for depths of 1.2 μm , 1.4 μm , and 1.6 μm , and packing ratios of 0.8, 0.9, and 1.0.

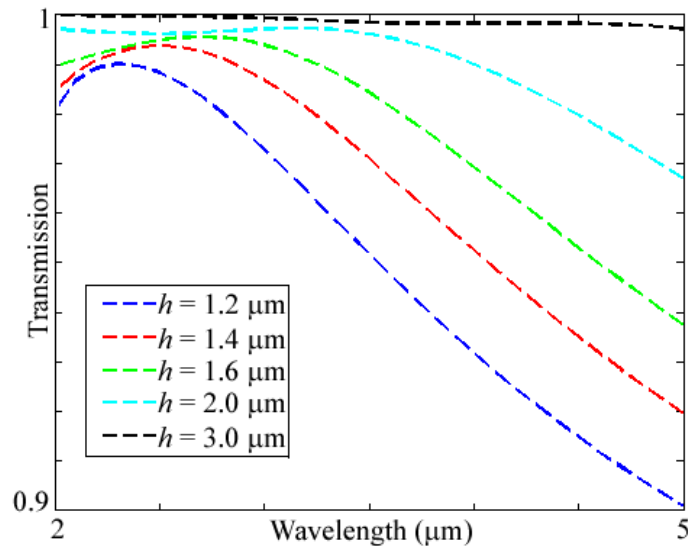


Fig. 17. Positive pyramid transmission for depths of 1.2 μm , 1.4 μm , 1.6 μm , 2.0 μm , and 3.0 μm . The packing ratio is 1.0.

We introduce a quantitative metric for evaluating these moth-eye structures: the mean (average) transmissivity for wavelengths between 2–5 μm . The average transmission for each structure is shown in Table 1. Using this metric, we find that positive pyramids of height 3.0 μm have an average transmissivity from 2–5 μm of 0.99878. Similarly, negative half-ellipsoids of

height 1.6 μm have an average transmissivity from 2–5 μm of 0.99885. While both structures can achieve similarly high performance, positive pyramids require much taller structures for optimal transmission.

Table 1. Average transmission for each structure type from 2–5 μm .

| Packing | Height (μm) | Positive pyramid | Negative half-ellipsoid |
|---------------|--------------------------|------------------|-------------------------|
| $w_2/s_x = 1$ | 1.2 | 0.95033 | 0.99452 |
| | 1.4 | 0.96518 | 0.99813 |
| | 1.6 | 0.97635 | 0.99885 |
| | 2.0 | 0.99011 | |
| | 3.0 | 0.99878 | |

Our results demonstrate that while these ideal cusp-like half-ellipsoid structures would perhaps be difficult to achieve exactly in practice, they can provide excellent performance with a reduced depth requirement compared to pyramid structures.

7. Conclusion

We have numerically studied moth-eye structures for increased coupling into and out of the endfaces of As_2S_3 chalcogenide optical fibers using both the RCWA and FDTD methods. We validated our theoretical model by comparing our results to experimentally-recorded results. We found we could obtain excellent agreement between theory and experiment.

We then investigated the effect of changing the size, shape, and packing of the moth-eye structures, as well as the angle-of-incidence for the input wave. We found that transmission generally increases when the structure, whether positive or negative, has a wide base width, a narrow tip width, and a large height or depth. We also found that the angle-of-incidence is an important parameter, and it should be taken into consideration when designing structures for multi-mode fibers.

Finally, we used these insights to design nearly ideal features that had a cusp-like shape. We found that, with the optimal parameters, negative half-ellipsoids and positive pyramids could be designed to achieve close to 99.9% transmission on average from 2–5 μm . We also found that negative half ellipsoids do not require as large a structure as positive pyramids for ideal transmission, which could make them easier to fabricate in practice.